CMS Physics Analysis Summary

Contact: cms-pag-conveners-top@cern.ch 2019/09/18

Template measurement of the top quark forward-backward asymmetry and anomalous chromoelectric and chromomagnetic moments in the semileptonic channel at $\sqrt{s} = 13$ TeV

The CMS Collaboration

Abstract

The linearized parton-level top quark forward-backward asymmetry $A_{\mathrm{FB}}^{(1)}$ and anomalous chromoelectric (d) and chromomagnetic (μ) moments are measured in 35.9 fb^{-1} of LHC proton-proton collision data collected with the CMS detector in 2016 at a center-of-mass energy 13 TeV. Candidate top quark/antiquark pair events decaying to lepton (muon or electron) plus jets final states with "resolved" (low energy) and "boosted" (high energy) topologies are selected and reconstructed using a kinematic fit of the decay products to top quark pair hypotheses. Parameters of interest are measured using binned likelihood fits to observed data of differential models based on extensions to tree-level cross sections for quark-antiquark and gluon-gluon initial states, and are determined to be $A_{\mathrm{FB}}^{(1)} = 0.048^{+0.088}_{-0.084}(\mathrm{stat}) \pm 0.028(\mathrm{syst})$, $d = 0.002 \pm 0.010(\mathrm{stat})^{+0.014}_{-0.019}(\mathrm{syst})$, and $\mu = -0.024^{+0.013}_{-0.007}(\mathrm{stat})^{+0.016}_{-0.006}(\mathrm{syst})$. The forward-backward asymmetry measured using this technique is directly comparable to similar quantities derived from Tevatron measurements.

1 Introduction

The top quark (t) is the heaviest known fundamental particle and has a mass that is close to the electroweak scale. The top quark's Yukawa coupling to the Higgs potential is close to unity, which suggests that the top quark may play a role in electroweak symmetry breaking. The top quark is also the only color triplet fermion that decays before it forms color singlet bound states. This permits the study of its fundamental interactions with gauge bosons without any of the complications caused by hadronization effects. In the standard model of particle physics (SM), top quarks are dominantly produced in pairs at the LHC via the strong interaction as described by Quantum Chromodynamics (QCD). Feynman diagrams for the leading order (LO) quark-antiquark ($q\bar{q}$) and gluon-gluon (gg) initiated subprocesses are shown in Fig. 1(a). Example diagrams for the next-to-leading order (NLO) quark-gluon (qg) initiated subprocess are shown in Fig. 1(b). NLO QCD calculations predict approximately 6% $q\bar{q}$, 69% gg, and 25% qg production of top quark pairs.

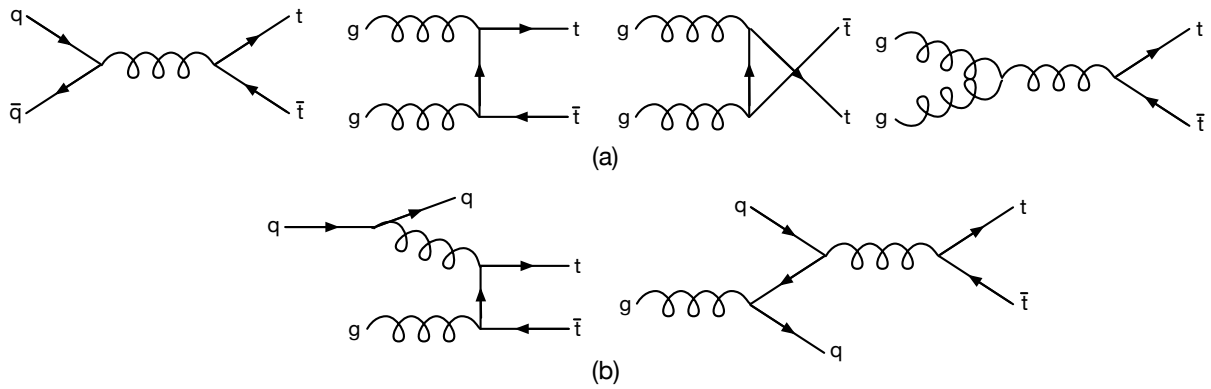

Figure 1: (a) Feynman diagrams for the leading order (LO) quark-antiquark ($q\bar{q}$) and gluon-gluon (gg) initiated subprocesses. (b) Example diagrams for the next-to-leading order (NLO) quark-gluon (qg) initiated subprocess.

In this note, we describe searches for anomalies in the angular distribution of produced $t\bar{t}$ pairs caused by modifications of the top-quark-antiquark-gluon ($t\bar{t}g$) interaction or by the presence of heavy states coupled to top quarks [1, 2]. These anomalies can be characterized by their effects on the distribution of $c^* = \cos\theta^*$ where θ^* is the production angle of the final state top quark with respect to the initial state parton direction in the $t\bar{t}$ center-of-mass (CM) frame. For those subprocesses that contain an initial state quark or antiquark, the sign of c^* follows from the relative directions of the initial state quark and final state top quark (or the initial state antiquark and final state top antiquark). We search separately for anomalies in the c^*-odd and the c^*-even distribution functions. The first search measures the top-quark forward-backward asymmetry, A_{FB}, and the second search measures the anomalous chromoelectric, d, and chromomagnetic, μ, dipole moments of the $t\bar{t}$ interaction vertex.

The parton-level forward-backward asymmetry is defined as

$$A_{\mathrm{FB}} = \frac{\sigma(c^* > 0) - \sigma(c^* < 0)}{\sigma(c^* > 0) + \sigma(c^* < 0)} \tag{1}$$

where $\sigma(c^* > 0)$ [$\sigma(c^* < 0)$] is the cross section for the production of the top quark in the forward [backward] hemisphere with respect to the incident quark direction. NLO effects in QCD

are expected to produce small positive values for A_{FB} measured in $\mathrm{q\bar{q}}$-initiated sub-processes [3–6].

The A_{FB} quantity was measured by the CDF and D0 experiments at the Tevatron, a proton-antiproton collider operating at center-of-mass energy 1.96 TeV, where the $\mathrm{q\bar{q}}$ subprocess dominated the $\mathrm{t\bar{t}}$ cross section. Initial measurements [7, 8] appeared to be significantly larger than NLO QCD expectation, however, more recent results [9–11] are consistent with the SM. Previous LHC measurements sensitive to the top quark angular production asymmetry performed by the CMS [12–15] and ATLAS [16, 17] Collaborations have focused on the top quark charge asymmetry A_{C} that does not isolate the $\mathrm{q\bar{q}}$ initial states from the gg and qg initial states and uses only a fraction of the available information.

The A_{FB} and A_{C} measurements done to date have been "model-independent", but this work represents a different approach in which a simplified model for the production mechanism is adopted, allowing the use of a likelihood analysis to isolate the $\mathrm{q\bar{q}}$ subprocess from the gg and qg subprocesses and from other backgrounds. The adopted model is a leading-order description of several possible beyond the SM processes [1, 2], and is a reasonable approximation for the expected NLO QCD effects [3]. The differential cross section for $\mathrm{q\bar{q}} \to \mathrm{t\bar{t}}$ can be expressed as a linear combination of symmetric and antisymmetric functions of the production angle and the antisymmetric function can be approximated as a linear function of c^*,

$$\frac{d\sigma}{dc^*}(\mathrm{q\bar{q}}) \simeq f_{\mathrm{sym}}(c^*) + \left[\int_{-1}^{1} f_{\mathrm{sym}}(x)dx\right] c^* A_{\mathrm{FB}}^{(1)} \tag{2}$$

where the symmetric function f_{sym} depends only on event kinematics and $A_{\mathrm{FB}}^{(1)}$ is a parameter. Using Eq. (2) to evaluate Eq. (1), we find that $A_{\mathrm{FB}} = A_{\mathrm{FB}}^{(1)}$ which we define to be the linearized forward-backward asymmetry. Equation (2) describes the leading order exchange and interference terms expected from s-channel resonances with chiral couplings. Fits of this expression to event samples generated with NLO QCD simulations yield values of $A_{\mathrm{FB}}^{(1)}$ that are within a few percent of A_{FB} values determined from event counting.

Several authors have considered the effects of possible top quark anomalous chromoelectric (d) and chromomagnetic (μ) dipole moments on the production of $\mathrm{t\bar{t}}$ final states at hadron colliders [18–21]. We follow the conventions and results of Ref. [20] and define d and μ in terms of the effective Lagrangian,

$$\mathcal{L}_{\mathrm{t\bar{t}g}} = -g_s \left[\bar{\mathrm{t}}\gamma^\mu G_\mu \mathrm{t} + i\frac{d}{2m_{\mathrm{t}}}\,\bar{\mathrm{t}}\sigma^{\mu\nu}\gamma_5 G_{\mu\nu}\mathrm{t} + \frac{\mu}{2m_{\mathrm{t}}}\,\bar{\mathrm{t}}\sigma^{\mu\nu}G_{\mu\nu}\mathrm{t}\right] \tag{3}$$

where t is the top quark field, $\sigma^{\mu\nu} = \frac{i}{2}[\gamma^\mu, \gamma^\nu]$, $G_\mu = G_\mu^a T^a$ with the gluon fields G_μ^a and the $SU(3)_C$ generators $T^a = \frac{1}{2}\lambda^a$ (a=1…8), and $G_{\mu\nu} = G_{\mu\nu}^a T^a$ with the gluon field strength tensors $G_{\mu\nu}^a = \partial_\mu G_\nu^a - \partial_\nu G_\mu^a - g_s f_{abc} G_\mu^b G_\nu^c$.

This note describes measurements of $A_{\mathrm{FB}}^{(1)}$, d and μ in proton-proton collision data at the CERN LHC. The analysis applies a template description of the total observed cross section to a sample of $\mathrm{t\bar{t}}$-enriched events collected by the CMS experiment in 2016 at $\sqrt{s} = 13$ TeV and corresponding to an integrated luminosity of 35.9 fb^{-1}. The analysis uses final states containing a single lepton (electron or muon) and several hadronic jets, called "lepton+jets," with three distinct topologies. The measurement of the $\mathrm{q\bar{q}}$ initial state top quark forward-backward asymmetry

is the first of its kind at the LHC and can be directly compared with results from the Tevatron experiments [7–11]. Values of the anomalous chromoelectric and chromomagnetic moments have previously been extracted from measurements of the $\mathrm{t\bar{t}}$ spin correlations [22]. This is the first measurement that relies on $\mathrm{t\bar{t}}$ differential distributions.

This note is organized as follows. Section 2 details the strategies used in extracting parameters of interest from the observed cross section. Section 3 describes the recorded and simulated data samples used in the analysis. Section 4 describes the event selection and kinematic reconstruction of the cross section observables. Section 5 describes the template method quantifying the fitting likelihood and techniques used to estimate the backgrounds. Section 6 describes the systematic uncertainties associated with the analysis. Section 7 describes the results of the fits to the data, and Section 8 provides a short summary.

2 Analysis strategy

Measuring the top quark forward-backward asymmetry at the LHC is considerably more challenging than at the Tevatron. The $\mathrm{t\bar{t}}$ cross section at the Tevatron is dominated by the $\mathrm{q\bar{q}}$ production subprocess and the incident quark and antiquark directions are reasonably well defined by the proton and antiproton beams. At the LHC, however, $\mathrm{t\bar{t}}$ production is dominated by the gg subprocess and the quark content of the initial state is symmetric. Since there can be no asymmetry from the gg initial state, these two effects significantly complicate the extraction of the asymmetry in the $\mathrm{q\bar{q}} \to \mathrm{t\bar{t}}$ subprocess. To isolate the $\mathrm{q\bar{q}}$ subprocess from the gg and qg subprocesses and from other backgrounds, we use the Drell-Yan variables ($m_{\mathrm{t\bar{t}}}$, x_F, c^*) to describe $\mathrm{t\bar{t}}$ events where $m_{\mathrm{t\bar{t}}}$ is the invariant mass of the $\mathrm{t\bar{t}}$ system and $x_F = 2p_{\mathrm{L}}/\sqrt{s}$ is the scaled longitudinal momentum p_{L} of the $\mathrm{t\bar{t}}$ system in the laboratory frame.

The distributions in ($m_{\mathrm{t\bar{t}}}$, x_F, c^*) for the gg, qg and $\mathrm{q\bar{q}}$ initial states can be visualized by considering a sample of $\mathrm{t\bar{t}}$ events simulated with the POWHEG v2 [23–25] Monte Carlo (MC) generator for pp collisions at $\sqrt{s} = 13\,\mathrm{TeV}$. The c^*, x_F, and $m_{\mathrm{t\bar{t}}}$ distributions for the three subprocesses are shown in Fig. 2; note that the gg and qg distributions are quite similar. Because the SM asymmetry for qg events is expected to be smaller than for $\mathrm{q\bar{q}}$ events [3], the gg and qg subprocesses are combined into a single distribution function for the purpose of this work. The $m_{\mathrm{t\bar{t}}}$ distribution for $\mathrm{q\bar{q}}$ events is somewhat narrower than for the other processes. The c^* distribution for $\mathrm{q\bar{q}}$ events is much flatter than that of the other processes due to the t-channel pole that dominates the gg and qg cross sections. Of key importance, the x_F distribution of the $\mathrm{q\bar{q}}$ events has a longer tail that helps to discriminate them and to correctly identify the incident quark direction. Because the gluon and antiquark parton distribution functions of the proton are much "softer" than the quark parton distribution functions, the direction of the $\mathrm{t\bar{t}}$ p_{L} is strongly correlated with the initial quark direction in $\mathrm{q\bar{q}}$ initiated events. This allows a reasonable determination of the initial parton direction to be made from the Collins-Soper frame [26], and the result of taking the longitudinal direction of the $\mathrm{t\bar{t}}$ pair in the lab frame as the quark direction is shown in Fig. 2. Defining N_C as the number of correct assignments and N_I as the number of incorrect assignments, the dilution factor $D = (N_C - N_I)/(N_C + N_I)$ is shown as a function of $|x_F|$; note that it becomes large in the $\mathrm{q\bar{q}}$ enriched region at large $|x_F|$.

In the CM frame, the differential cross section for the process $\mathrm{q\bar{q}} \to \mathrm{t\bar{t}}$ can be written as

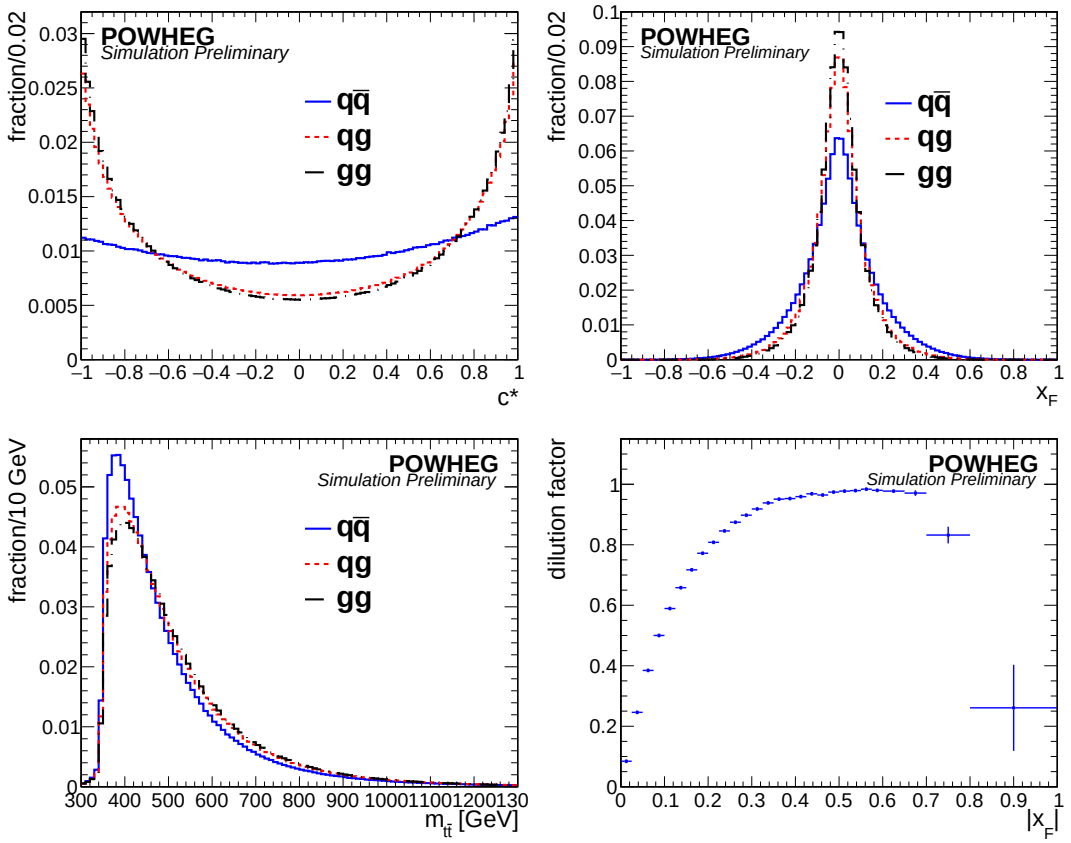

Figure 2: The generator-level c^* (top left), x_F (top right), and $m_{t\bar{t}}$ (bottom left) distributions for the subprocesses $q\bar{q}/qg/gg \to t\bar{t}$. The result of taking the longitudinal direction of the $t\bar{t}$ pair in the lab frame as the quark direction for $q\bar{q}$ events is shown in the bottom right plot.

$$\frac{d\sigma}{dc^*}(q\bar{q}) = K\frac{\pi\alpha_S^2}{9m_{t\bar{t}}^2}\beta\left\{2-\beta^2+\beta^2c^{*2}+\alpha\left(1-\beta^2c^{*2}\right)+2\left[2-\frac{2}{3}\beta^2+\alpha\left(1-\frac{1}{3}\beta^2\right)\right]A_{FB}^{(1)}c^*\right\} \tag{4}$$

where: K is an NLO normalization factor, $\alpha_S = g_s^2/4\pi$ is the strong coupling parameter, $\beta = \sqrt{1-4m_t^2/m_{t\bar{t}}^2}$ is the velocity of the t in the CM frame, m_t is the top quark rest mass, and $\alpha = \alpha(\beta)$ is the longitudinal polarization of the exchanged gluon. This parameterization describes SM $q\bar{q} \to t\bar{t}$ generation to NLO precision, with an extension allowing for a general linear forward-backward asymmetry approximated at LO.

At leading order, the presence of d and μ modify both $q\bar{q}$ and gg initiated parts of the $pp \to t\bar{t}$ cross section. As in the case of the forward-backward asymmetry, we use a framework that describes the SM NLO contributions empirically and possible anomalous contributions at LO. The $q\bar{q}$ cross section can then be expressed as follows [20]

$$\frac{d\sigma}{dc^*}(q\bar{q}) = K\frac{\pi\alpha_S^2}{9m_{t\bar{t}}^2}\beta\left\{2-\beta^2+\beta^2c^{*2}+\alpha\left(1-\beta^2c^{*2}\right)+4(2\mu+\mu^2-d^2)+4\left(\mu^2+d^2\right)\frac{1-\beta^2c^{*2}}{1-\beta^2}\right\} \tag{5}$$

where the last term is strongly enhanced at large pair mass (large β). The gg cross section can be expressed as follows,

$$\frac{d\sigma}{dc^*}(gg) = K\frac{\pi\alpha_S^2\beta}{48m_{t\bar{t}}^2}\left\{\frac{7+9\beta^2c^{*2}}{1-\beta^2c^{*2}}\left[\frac{1-\beta^4c^{*4}+2\beta^2(1-\beta^2)(1-c^{*2})}{2(1-\beta^2c^{*2})}\left(1+\varepsilon\beta^2c^{*2}\right)+\mu(1+\mu)\right]\right.$$
$$\left.+8(\mu^2+d^2)\left(\frac{7(1+\mu)}{1-\beta^2}+\frac{1-5\mu}{2(1-\beta^2c^{*2})}\right)+8(\mu^2+d^2)^2\left(\frac{1}{1-\beta^2c^{*2}}+\frac{1}{1-\beta^2}+\frac{4(1-\beta^2c^{*2})}{(1-\beta^2)^2}\right)\right\} \quad (6)$$

where the SM NLO contributions are parameterized by the functions K and $\varepsilon = \varepsilon(\beta)$. As in the $q\bar{q}$ case, the effects of the anomalous moments are largest at large pair mass.

Because the effects of heavy unobserved states and non-zero anomalous dipole moments are largest at large pair mass, and because the fraction of $q\bar{q}$ events increases with top quark pair momentum, the first of the three considered $t\bar{t}$ decay topologies comprises very massive events in which the top quark decay products are fully merged into single jets. The second topology considers events of lower pair mass in which the decay products are partly merged, bridging the gap between events identifiable as either fully merged or fully resolved. These first two topologies are collectively referred to as "boosted" because their decaying top quarks have high p_T. Finally, the third and most populated category includes the lowest mass events, called "resolved" events because all decay products are individually distinguishable. The selected event sample comprises approximately 2.2% type-1, 11.6% type-2, and 86.2% type-3 events.

As detailed in Section 5, linear combinations of templates stored as three-dimensional histograms in $m_{t\bar{t}}$, x_F, and c^* are used in a simultaneous likelihood fit to the observed differential cross section across 12 total channels separated by decay topology and lepton charge and flavor. Truth information from simulated SM $t\bar{t}$ events generated at NLO is used to separate $q\bar{q}$ from qg/gg events and reweight them to produce individual contributions to the cross section hypotheses in Equations (4), (5), and (6). Other MC and data events are used to build templates representing background contributions, and the total general linear combination is fit to data three times independently to extract values of $A_{FB}^{(1)}$, d, and μ.

3 Data and simulation

This analysis has been performed using the data sample collected with the CMS detector in 2016 at a center-of-mass energy of 13 TeV, corresponding to an integrated luminosity of $35.9 \pm 0.9\,\text{fb}^{-1}$ [27]. Events analyzed in the boosted channels are those passing a single-muon trigger requiring a muon with $p_T > 50$ GeV, a single-electron trigger requiring an electron with $p_T > 115$ GeV, or an electron+jets trigger with 50 and 165 GeV thresholds on electron and leading jet p_T respectively. Events analyzed in the low-p_T resolved channels are those passing a single-muon trigger requiring an isolated muon with $p_T > 24$ GeV, or a single-electron trigger requiring an electron with $p_T > 27$ GeV.

The POWHEG v2 [23–25] MC generator is used to simulate the signal $t\bar{t}$ process [28] at NLO with the PYTHIA 8.219 parton shower generator [29] using the CUETP8M2T4 tune [30] at a top quark mass $m_t^{MC} = 172.5$ GeV. This sample also models [31] dependence on renormalization and factorization scales $\mu_R = \mu_F = m_T = \sqrt{m_t^2 + p_T^2}$ as they are halved or doubled [32, 33], and

on the choice of the parton distribution function (PDF) set NNPDF3.0 [34] with strong coupling $\alpha_S = 0.118$ to describe the proton substructure.

POWHEG and PYTHIA with the same tune are also used to simulate contributions to the background from single top quark processes at NLO, both in the t channel [35] with POWHEG v2 and madspin [36] and in tW with POWHEG v1 [37]. Background contributions from single top quark processes in the s channel are simulated using the MC@NLO MC generator [38] matched to PYTHIA 8 parton showers, and contributions from Drell-Yan (Z/γ+jets) and W+jets production at NLO are simulated using the MADGRAPH5_aMC@NLO v2.3.3 MC generator [39] matched using the MLM prescription [40] to PYTHIA 8 parton showers with tune CUETP8M1.

Events in every MC sample are processed through a full simulation of the CMS detector in GEANT4 [41]. MC samples used are normalized to their predicted cross sections at NLO for single top quark production in the s and t channels [42], at NLO plus next-to-next-to-leading logarithms (NNLL) for single top quark production in tW [43], at next-to-next-to-leading order (NNLO) for W+jets and Z/γ+jets [44], and at NNLO+NNLL for the $\mathrm{t\bar{t}}$ signal [45]. All MC samples used have been corrected to bring the generated pileup into agreement with the observed distribution in data. Identical selection criteria and reconstruction procedures are otherwise applied to all real and simulated data events.

4 Event selection and reconstruction

Events are selected based on three different "single-leptonic" $\mathrm{t\bar{t}}$ decay topologies, in which one member of the top quark pair decays to a charged lepton, a neutrino, and a single hadronic jet and the other decays only to hadronic jets. "Type-1" events are those identified to have top quark pairs decaying with very high momentum, such that the hadronically-decaying top quark's three constituent jets merge into one large jet. "Type-2" events are those for which the presence of a large, high-momentum, high-mass jet indicates either a partially- or fully-merged hadronic top quark decay, but which lack a single large jet sufficiently likely to have originated from a top quark decay. "Type-3" events are relatively lower mass events in which the hadronically-decaying top quark appears as three small and individually resolved jets. Events with a single lepton (electron or muon) and a jet configuration corresponding to one of the three hadronic decay topologies are selected, resulting in six mutually exclusive categories: one each for type-1, type-2, and type-3 e+jets and μ+jets.

Muon (electron) candidates are required to have $p_{\mathrm{T}} > 50(80)$ GeV in the boosted regions, and $p_{\mathrm{T}} > 30$ GeV in the resolved regions. Only lepton candidates in the pseudorapidity range $|\eta| < 2.4$ are considered, and any electron candidates in the transition region between barrel and endcap calorimeter, corresponding to $1.44 < |\eta| < 1.57$, are rejected. To ensure that leptons observed in an event correspond to particles in the final decay state rather than products of hadronization, leptons are required to be isolated from nearby hadronic activity in the event. Lepton isolation in boosted events is determined with the use of a "2D cut" applied as a logical OR of two independent cuts on the lepton's relative transverse momentum $p_{\mathrm{T}}^{\mathrm{rel}}$ and ΔR with respect to its nearest AK4 jet with $p_{\mathrm{T}} > 15$ GeV and $|\eta| < 3.0$. In order to be considered isolated in the boosted regions, a lepton must have $p_{\mathrm{T}}^{\mathrm{rel}} > 30$ or $\Delta R > 0.4$. In the resolved regions, a lepton candidate's isolation is additionally determined according to the scalar sum of the p_{T} of neutral and charged hadron PF candidates within a cone of size $\Delta R = 0.4(0.3)$ for muons (electrons). This sum is required to be less than 15% (6%) of the muon (electron) p_{T}, and only leptons passing both the 2D cut and these PF isolation criteria are considered isolated in the resolved regions. Any event containing more than one isolated lepton is rejected to suppress background from "dileptonic" $\mathrm{t\bar{t}}$ decays in which both top quarks decay to leptons. Require-

ments are also imposed on the p_T^{miss} in each event to suppress background from QCD multijet processes: events with a muon (electron) in the boosted regions require $p_T^{miss} > 50(100)$ GeV, and resolved events of both lepton flavors require $p_T^{miss} > 40$ GeV. Events failing p_T^{miss} requirements and/or lepton isolation requirements are used in the data-driven estimation of QCD multijet background contribution as described in Section 5.

All AK4 (AK8) jets considered are required to have $p_T > 30(200)$ GeV in the range $|\eta| < 2.4$. AK8 jets are also required to have at least two sub jets as identified by the SD declustering algorithm. In type-1 events, at least one AK8 jet must be present that is identified ("tagged") as originating from the merged hadronic decay of a top quark. These top quark tagged (t-tagged) jets are selected using simultaneous criteria on jet p_T, jet mass after soft-drop application, and the ungroomed N-subjettiness [46] substructure discriminant variable $\tau_{32} = \tau_3/\tau_2$ for which smaller values indicate greater likelihood that the jet is composed of three rather than two subjets. An AK8 jet is considered t-tagged if it has $p_T > 400$ GeV, softdrop mass in the range $105 < m_{AK8}^{SD} < 220$ GeV, and $\tau_{32} < 0.81$. By contrast, type-2 events are required to have zero t-tagged AK8 jets, but must contain at least one AK8 jet with $m_{AK8}^{SD} > 40$ GeV and at least four AK4 jets. Type-1 and type-2 muon (electron) events require the highest momentum AK4 jet to have $p_T > 150(250)$ GeV and the second-highest momentum AK4 jet to have $p_T > 50(70)$ GeV. Type-3 events are required to contain at least four AK4 jets.

To aid in discrimination of $t\bar{t}$ signal over Z/γ+jets and W+jets background, AK4 jets originating from decays of b quarks are tagged using an algorithm that combines lifetime information from tracks and secondary vertices [47]. Type-1 and type-2 events require at least one AK4 jet that is b quark tagged (b-tagged) at the "loose" working point of the algorithm, which has an 83% efficiency of correctly identifying a b quark jet and a 9% probability of misidentifying a light quark jet as a b quark jet (mistag rate). Type-3 events require at least two AK4 jets tagged at the "medium" working point of the algorithm with a b tagging efficiency of 63% and a 1% mistag rate.

The top quark pair kinematic quantities are reconstructed from their constituent decay products using a maximum likelihood estimation fit [48, 49], which allows the momenta of the decay products to vary within their resolutions and iterates over all possible assignments of jets to either the hadronic or leptonic side of the top quark pair decay, determining the most likely value of the unknown neutrino longitudinal momentum and the best possible assignment of jets to conform with the decay hypothesis. In type-1 events, the hadronically decaying top quark is assumed to be represented by the t-tagged AK8 jet and the possible AK4 jet assignment hypotheses are all assignments of b-tagged AK4 jets to the leptonic side of the decay that result in a leptonic top quark candidate (lepton plus p_T^{miss} plus AK4 jet) separated from the t-tagged AK8 jet by $\Delta R(t_{had}, t_{lep}) > 2$. Type-2 and type-3 events ignore AK8 jets entirely in their reconstruction, and instead assign each of the four or five AK4 jets with the highest p_T either to the leptonic or hadronic side of the decay, or neither, with b-tagged jets in place.

For each event, the hypothesis resulting in the smallest fit χ^2 (negative log likelihood) value is chosen to represent the complete top quark pair decay, and the leptonic/hadronic-side top quarks are reconstructed as the vector sums of their decay particles' rescaled four-momenta. This kinematic fitting procedure is highly effective, returning the correct hypotheses in 98%, 80%, and 73% of type-1, type-2, and type-3 semileptonic $t\bar{t}$ MC events respectively for which a particle-matched hypothesis exists.

After reconstruction of the $t\bar{t}$ pair, type-1 and type-2 events are further required to have reconstructed leptonic top quark mass $m_{t,lep}^{reco} < 210$ GeV, and $\chi^2 < -15$. The inversion of either of these criteria is used to form a control region constraining the cross section of the W+jets

background process as described in Section 5. Figures 3, 4, and 5 show comparisons of reconstructed c^*, $|x_F|$, and $m_{\mathrm{t\bar{t}}}$ for selected MC and data events in the lepton charge-summed type-1, type-2, and type-3 regions, including QCD multijet background estimated using the data-driven method discussed in Section 5.

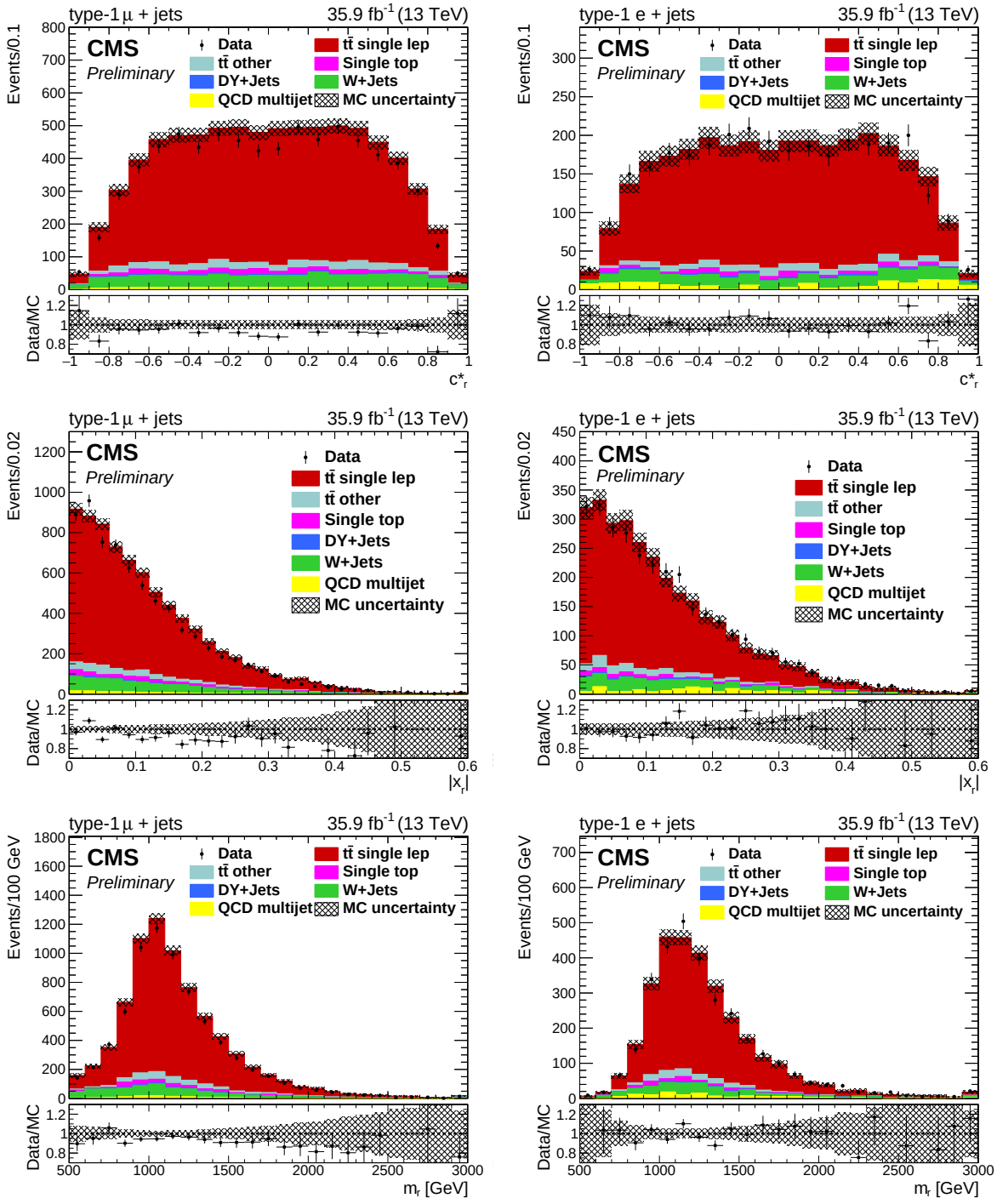

Figure 3: Data/MC comparison of reconstructed c_{r}^{*} (top), $|x_{\mathrm{r}}|$ (middle), and m_{r} (bottom) for events passing full type-1 μ+jets (left column) and e+jets (right column) selection criteria. The MC signal and background show their nominal, pre-fit predictions, and the MC uncertainty pictured in the hatched bands represents statistical errors only. Contribution from QCD multijet background is estimated using the data-driven method described in Section 5. The lower panels of each figure show the ratio of the observed data and total prediction in each bin.

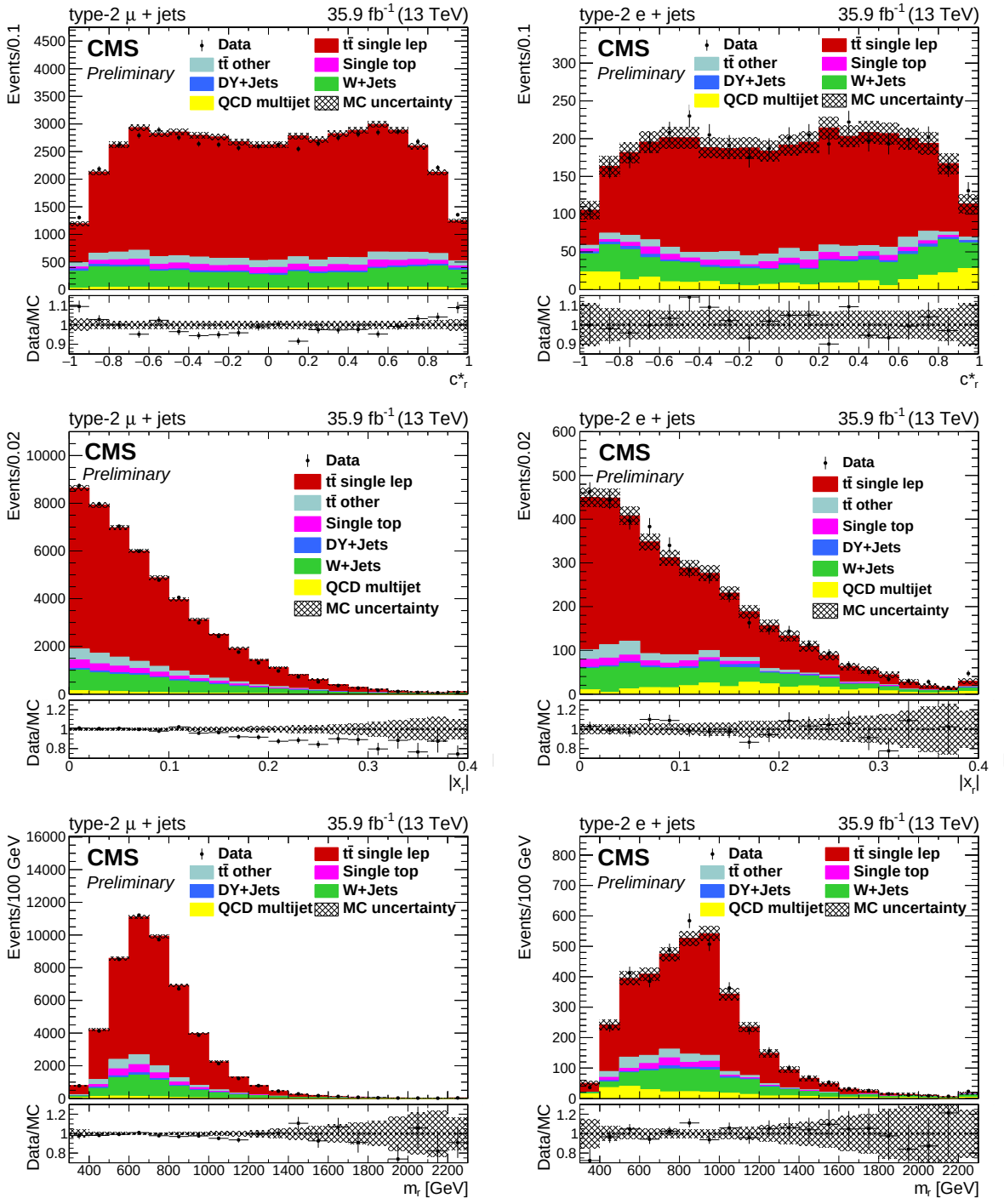

Figure 4: Data/MC comparison of reconstructed c_{r}^{*} (top), $|x_{\mathrm{r}}|$ (middle), and m_{r} (bottom) for events passing full type-2 μ+jets (left column) and e+jets (right column) selection criteria. The MC signal and background show their nominal, pre-fit predictions, and the MC uncertainty pictured in the hatched bands represents statistical errors only. Contribution from QCD multijet background is estimated using the data-driven method described in Section 5. The lower panels of each figure show the ratio of the observed data and total prediction in each bin.

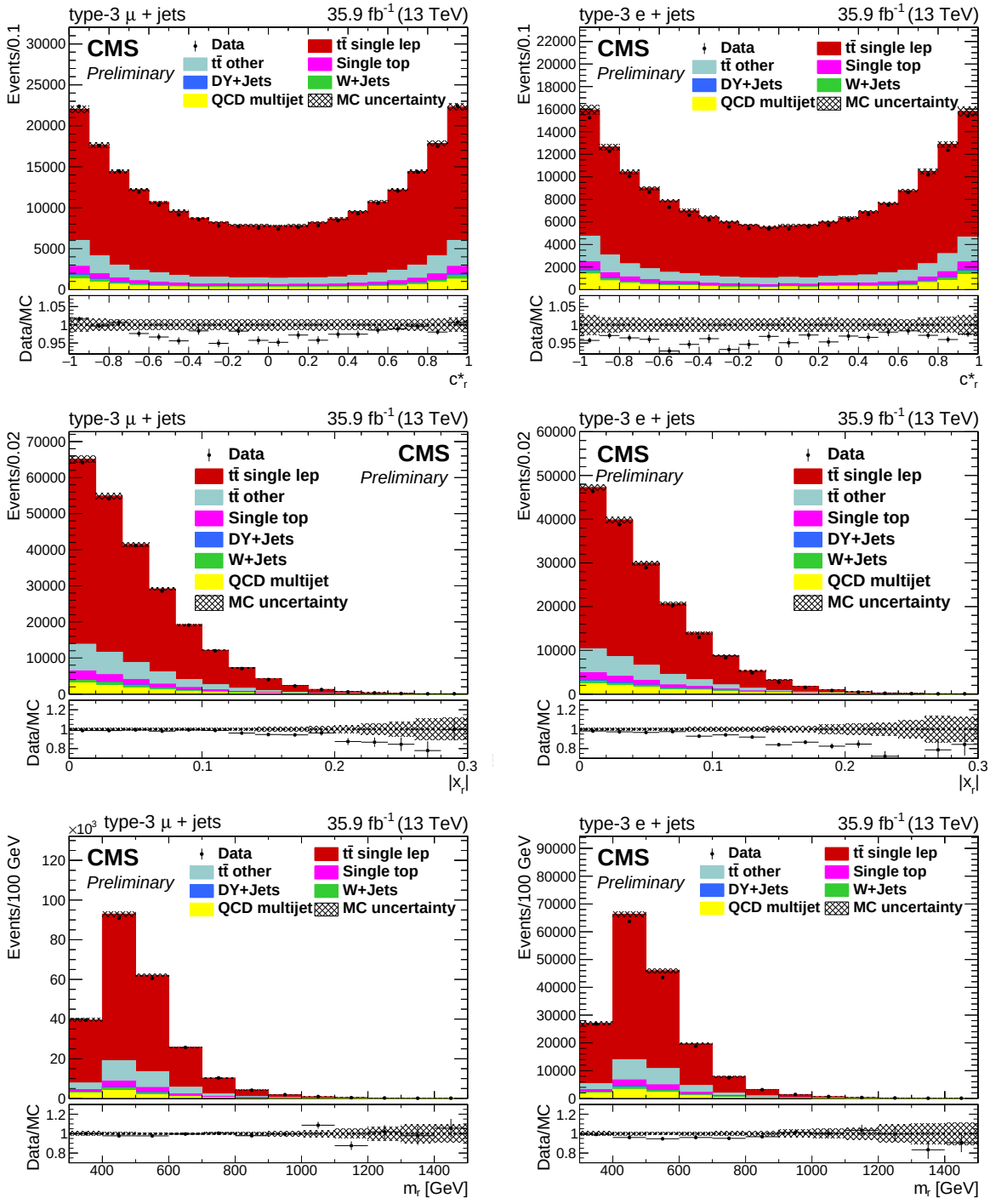

Figure 5: Data/MC comparison of reconstructed c_r^* (top), $|x_r|$ (middle), and m_r (bottom) for events passing full type-3 μ+jets (left column) and e+jets (right column) selection criteria. The MC signal and background show their nominal, pre-fit predictions, and the MC uncertainty pictured in the hatched bands represents statistical errors only. Contribution from QCD multijet background is estimated using the data-driven method described in Section 5. The lower panels of each figure show the ratio of the observed data and total prediction in each bin.

5 Template building and background estimation

The analysis is performed by reconstructing the triplet of Drell-Yan variables (m_{r}, x_{r}, c_{r}^{*}) from lepton+jets events in which the sign of the lepton tags the final state top quark/antiquark direction and the direction of the pair along the beam axis can be taken as the likely quark direction. To accommodate the $\mathrm{t\bar{t}}$ transverse momentum of the measured and simulated events, the Collins-Soper frame [26] is adopted to define the reconstructed angle c_{r}^{*}. The SM $\mathrm{t\bar{t}}$ distributions are determined from events simulated at NLO. The distribution functions representing extensions to the SM are determined by reweighting the NLO simulated events using the approximate NLO analytic expressions given in Eqs. (4), (5), and (6) for the numerators and denominators of the reweighting functions.

To measure $A_{\mathrm{FB}}^{(1)}$, the detector is assumed to have the same efficiency for reconstructing tracks of positively- and negatively-charged particles in the same configuration. This implies a charge-parity symmetry where the acceptance for an event with a positively-charged lepton and angles (c^{*}, c_{r}^{*}) is the same as that for a negatively-charged lepton with angles ($-c^{*}$, $-c_{\mathrm{r}}^{*}$). To exploit this symmetry, a fourth reconstructed quantity, the lepton charge Q, is used to describe each event. The 4D distribution function $f(\vec{y})$ of the reconstructed variables $\vec{y} = (m_{\mathrm{r}}, c_{\mathrm{r}}^{*}, x_{\mathrm{r}}, Q)$ is determined from fully simulated and reconstructed events and from empirically determined reconstructed background events,

$$f(\vec{y}) = \sum_{j} R_{\mathrm{bk}}^{j} f_{\mathrm{bk}}^{j}(\vec{y}) + \left\{ \left(1 - R_{\mathrm{q\bar{q}}}\right) f_{\mathrm{gg}}(\vec{y}) + R_{\mathrm{q\bar{q}}} \left[f_{\mathrm{qs}}(\vec{y}) + A_{\mathrm{FB}}^{(1)} f_{\mathrm{qa}}(\vec{y}) \right] \right\} \tag{7}$$

where: $f_{\mathrm{bk}}^{j}(\vec{y})$ represent normalized distribution functions for several backgrounds; R_{bk}^{j} are matching background fraction scale factors; $R_{\mathrm{q\bar{q}}}$ is the fraction of $\mathrm{t\bar{t}}$ events that are categorized as $\mathrm{q\bar{q}}$ initiated; $f_{\mathrm{gg}}(\vec{y})$ is the normalized distribution function for gg, qg, qq, $\mathrm{\bar{q}\bar{q}}$, and $\mathrm{q_i\bar{q}_j}$ (where i, j label flavors and $i \neq j$) initiated events; $f_{\mathrm{qs}}(\vec{y})$ is the symmetrized distribution for $\mathrm{q\bar{q}}$ initiated events, and $f_{\mathrm{qa}}(\vec{y})$ is the antisymmetrized linearized distribution for $\mathrm{q\bar{q}}$ initiated events. The symmetrized function is created by incrementing bins at (c_{r}^{*}, Q) and ($-c_{\mathrm{r}}^{*}$, $-Q$) for each generated event and contains a full NLO description of the process. The antisymmetrized linearized function follows from Eq. (4) by accumulating the event weight

$$w_{\mathrm{qa}}(m_{\mathrm{t\bar{t}}}^{2}, c^{*}) = \frac{2\left[2 - \frac{2}{3}\beta^{2} + \alpha(1 - \frac{1}{3}\beta^{2})\right] c^{*}}{2 - \beta^{2} + \beta^{2}c^{*2} + \alpha\left(1 - \beta^{2}c^{*2}\right)} \tag{8}$$

in the bin at (c_{r}^{*}, Q) and $w_{\mathrm{qa}}(m_{\mathrm{t\bar{t}}}^{2}, -c^{*})$ in the mirror bin at ($-c_{\mathrm{r}}^{*}$, $-Q$). Note that these distribution functions or templates are independent of any of the parameters to be determined. This technique directly determines the average parton-level linearized asymmetry and automatically accounts for resolution, dilution, migration, and acceptance effects so long as they are correctly modeled in the simulation. The templates representing well-simulated background contributions can likewise be populated with simulated events.

Equations (5) and (6) are used to define a 4D distribution function in terms of eight parameter-independent template functions,

$$f(\vec{y}) = \sum_j R^j_{\mathrm{bk}} f^j_{\mathrm{bk}}(\vec{y}) + \left\{ \frac{(1 - R_{\mathrm{q\bar{q}}})}{F_{\mathrm{gg}}(\mu, d)} \Big[f_{\mathrm{g0}}(\vec{y}) + \mu(1+\mu) f_{\mathrm{g1}}(\vec{y}) \right.$$
$$+ (\mu^2 + d^2)(1+\mu) f_{\mathrm{g2}}(\vec{y}) + (\mu^2 + d^2)(1 - 5\mu) f_{\mathrm{g3}}(\vec{y}) + (\mu^2 + d^2)^2 f_{\mathrm{g4}}(\vec{y}) \Big]$$
$$\left. + \frac{R_{\mathrm{q\bar{q}}}}{F_{\mathrm{q\bar{q}}}(\mu, d)} \Big[f_{\mathrm{q0}}(\vec{y}) + \left(2\mu + \mu^2 - d^2\right) f_{\mathrm{q1}}(\vec{y}) + \left(\mu^2 + d^2\right)) f_{\mathrm{q2}}(\vec{y}) \Big] \right\} \quad (9)$$

where the template functions $f_{\mathrm{qi}}(\vec{y})$ and $f_{\mathrm{gi}}(\vec{y})$ are constructed from simulated $\mathrm{t\bar{t}}$ events using weights described in Appendix A and the normalization functions $F_{\mathrm{q\bar{q}}}$ and F_{gg} ensure that the $\mathrm{q\bar{q}}$ and gg normalizations are independent of the parameters d and μ.

The distribution functions in Eqs. (7) and (9) are fit to data as sets of "templates": three-dimensional histograms in reconstructed top quark pair $(m_{\mathrm{r}}, x_{\mathrm{r}}, c^*_{\mathrm{r}})$ separated by lepton charge Q. The template histograms are binned differently in each channel, using variable bin widths in each dimension. Each channel's binning scheme is designed to maximize sensitivity to the parameters of interest while maintaining a sufficient number of observed data events in each bin so that statistical fluctuations and systematic uncertainties do not dominate the numerical minimization. Templates are unrolled into one-dimensional distributions as functions of global bin number before fitting.

The $f_{\mathrm{qs}}(\vec{y})$, $f_{\mathrm{qa}}(\vec{y})$, $f_{\mathrm{gg}}(\vec{y})$, $f_{\mathrm{qi}}(\vec{y})$, and $f_{\mathrm{gi}}(\vec{y})$ templates are constructed by accumulating single-leptonic $\mathrm{t\bar{t}}$ MC events in each bin, reweighted so as to factorize out parameters of interest (i.e., with the weight in Eq. (8) used for $f_{\mathrm{qa}}(\vec{y})$, and the weights in Appendix A used for $f_{\mathrm{qi}}(\vec{y})$ and $f_{\mathrm{gi}}(\vec{y})$). These templates along with $f^j_{\mathrm{bk}}(\vec{y})$, describing background contributions, are summed in a linear combination to estimate the total observed cross section.

The background processes contributing to this analysis are dileptonic and all-hadronic $\mathrm{t\bar{t}}$, single top, Drell-Yan Z/γ+jets, W+jets, and QCD multijet processes. Background contributions other than QCD multijet are estimated using MC predictions after corrections are applied to account for identification and selection efficiency differences between simulation and data. The top quark and Z/γ+jets backgrounds make relatively small contributions, and are considered together as one set of background templates $f^1_{\mathrm{bk}}(\vec{y})$.

The W+jets background process is accounted for by a dedicated set of background templates $f^2_{\mathrm{bk}}(\vec{y})$ because its production cross section is less precisely known from theory. For the type-1 and type-2 regions the amount of W+jets background is constrained by performing a simultaneous fit to data in orthogonal control regions selected to be enriched in W+jets events. The control regions are populated by events that are otherwise selected as described in Section 4, but which fail either of the requirements on kinematic fit χ^2 or reconstructed leptonic top quark mass: a logical OR of $m^{\mathrm{reco}}_{\mathrm{t,lep}} \geq 210\,\mathrm{GeV}$ and $\chi^2 \geq -15$. This selection was chosen by comparing simulated semileptonic $\mathrm{t\bar{t}}$ and W+jets events; W+jets events consistently exhibit larger values of kinematic fit χ^2 and have leptonic top quark masses that are less resolved around the true top quark mass than semileptonic $\mathrm{t\bar{t}}$ events.

The QCD multijet background contribution is not well described by the simulation due to a lack of simulated events that pass full selection criteria, and so QCD multijet background is estimated using a data-driven method called "ABCD sidebanding," which incorporates information from multiple orthogonal selection sidebands in the two-dimensional space of lepton isolation and $p^{\mathrm{miss}}_{\mathrm{T}}$. The "C" sideband region contains events that are otherwise selected except

that their leptons are not isolated. The "A" and "B" sideband regions both contain events that fail $p_{\mathrm{T}}^{\mathrm{miss}}$ requirements, and events in the "A" ("B") region fail (pass) lepton isolation selection criteria. The QCD multijet background shapes are determined by subtracting non-QCD MC contamination from observed data in the "C" sideband, resulting in a subsample enhanced in QCD multijet background. This MC subtraction from data leaves behind the expected QCD multijet background contribution, and is repeated in the "B" and "A" sidebands. Transfer factors are calculated in each channel and region by taking the ratios of the total numbers of expected QCD multijet background events in the "B" sidebands to the "A" sidebands, which approximates the efficiencies for the shapes observed in the "B" sidebands to be transferred to the full signal region. The transfer factor values are approximately 0.004 (0.46), 0.003 (0.35), and 0.37 (1.44) in the type-1, type-2, and type-3 signal region μ(e)+jets channels respectively. This procedure is performed independently in all signal and W+jets control regions to yield the set of QCD multijet background templates $f_{\mathrm{bk}}^{3}(\vec{y})$.

6 Systematic uncertainties and measurement

Systematic uncertainties in the normalization and/or shape of the templates used in fitting are introduced from a variety of sources and statistically accounted for using nuisance parameters constrained with priors as described in Section 7. Sources of systematic uncertainty and their methods of accounting are listed below and summarized in Table 1.

Jet energy corrections: Jet energies and their resolutions are corrected in the simulation to agree with observations in data. These corrections are achieved by application of a jet energy scale (JES) dependent on pileup as well as jet p_{T}, η, energy, and area, and a smearing of the jet energy resolution (JER) dependent on jet $|\eta|$. The JES and JER factors are independently varied up and down as they are applied to AK4 and AK8 jets simultaneously, including propagation of the corrections to the observed $p_{\mathrm{T}}^{\mathrm{miss}}$.

Pileup: Uncertainties in the procedure used for reweighting the pileup distribution in the simulation are accounted for by varying the inelastic pp cross section $\pm 4.6\%$.

Trigger and lepton ID/isolation efficiencies: Trigger efficiencies in data and simulation are determined using multiple independent methods, each resulting in a lepton p_{T}- and η-dependent scale factor applied to simulated events. The different algorithms for determining lepton identification and isolation also result in their own sets of pileup- and lepton p_{T}- and η-dependent scale factors. The average values of the scale factors applied are about 0.94 (0.96) for boosted (resolved) μ+jets events and about 0.98 for boosted and resolved e+jets events. Uncertainties in these scale factors are retained and their independent overall up and down variation effects are propagated to templates event-by-event.

b tagging efficiency: Scale factors dependent on jet flavor, p_{T}, and η are applied to simulated events to correct for differences in b tagging efficiency and mistag rate between data and simulation. Their uncertainties are retained and propagated to templates independently for each jet flavor type and b tagging algorithm working point.

top tagging efficiency: Three data/MC efficiency scale factors with associated systematic uncertainties are applied to all simulated events selected with top quark tagged jets to correct for differences in tagging efficiency between data and simulation. The three factors are applied according to whether a particular jet is fully, partially, or not merged as determined by a MC matching procedure, and are dependent on jet p_{T}.

top quark p_T reweighting: Recent NNLO QCD + electroweak calculations of top quark pair production [50] describe how NNLO effects impact the top quark and antiquark p_T spectra in ways for which NLO generators cannot account. Scale factors dependent on generated top quark and antiquark p_T are calculated and applied to bring the generated p_T distributions into agreement with those predictions and the uncertainties in the calculated scale factors are considered a systematic uncertainty [51].

PDF and strong coupling variation: The systematic uncertainty due to the choice of the NNPDF3.0 PDF set used in generating $t\bar{t}$ MC events is accounted for using the $\pm 1\sigma$ deviations observed across 100 per-event weights corresponding to PDF set variations in a Gaussian distribution [34]. Variations in α_S are accounted for by recalculating the generated event weight with $\alpha_S = 0.118 \pm 0.0015$ [52]. This uncertainty is combined in quadrature with the overall PDF uncertainty to give one set of PDF/α_S up/down templates [53, 54].

Renormalization and factorization scales: Modeling uncertainties in the matrix element generation process are accounted for by reweighting simulated events to match event shape distributions generated with μ_R and μ_F varied up (down) by a factor of 2 (0.5), both independently and together, resulting in three nuisance parameters describing μ_R, μ_F, and combined μ_R-μ_F scale variations [32, 33].

Parton shower radiation/matching scales and underlying event uncertainty: Uncertainties in initial and final state radiation and matrix element to parton shower matching scales, as well as uncertainties due to the choice of CUETP8M2T4 tune for the $t\bar{t}$ simulation, are accounted for using templates built from independent MC samples generated with relevant PYTHIA parameters varied within their uncertainties [30]. These samples are processed identically to signal MC samples, and their resulting templates are smoothed to reduce bias from statistical noise before fitting.

Color reconnection modelling: Systematic uncertainties due to choice of color reconnection model are accounted for using a single set of up/down variation templates that are constructed as an envelope of the average fractional shifts observed in each bin of templates built from independent MC samples corresponding to three different color reconnection hypotheses. These templates are also smoothed before fitting.

b fragmentation and semileptonic branching ratio: Uncertainties in the b quark fragmentation and semileptonic branching ratio are accounted for using per-event scale factors dependent on the generator-level transfer function $x_b = p_T(B)/p_T(b \text{ jet})$ for fragmentation and on the ratios of theoretical to PYTHIA branching ratios for branching ratio uncertainties.

Luminosity uncertainty: The total analyzed integrated luminosity's $\pm 2.5\%$ uncertainty [27] is accounted for as a single nuisance parameter with a log-normal prior correlated across all analysis channels.

Process yields: A $\pm 1\%$ uncertainty on the fraction of semileptonic top quark pair production due to quark-antiquark annihilation is included as a nuisance parameter affecting the shape of $t\bar{t}$ signal templates. A $\pm 10\%$ uncertainty is assigned to the cross section of W+jets processes, scaling all $f^2_{bk}(\vec{y})$ templates.

Data-driven QCD multijet background estimate transfer factors: The statistical uncertainty in each analysis channel's data-driven QCD multijet background estimate transfer factor is modeled by several independent variation nuisances, one for each estimate that is made.

Finite MC generation: The statistical fluctuations in MC predictions are accounted for

using the "Barlow-Beeston" method [55], which adds a Poisson uncertainty to each template bin's cumulative contents.

Table 1: List of nuisance parameters considered in fits to data. "N" stands for "normalization" and "S" for "shape" in the "type" column. The "Scale" column lists the absolute value of the associated fractional up/down shifts averaged over all affected template bins. $R_{\text{QCD}}^{t/C/R}$ indicated that the QCD multijet yield uncertainties are independent in each topology t, channel C, and region R.

Nuisance source	**Uncertainty**	**Type**	**Scale**	**Affects**
Jet Energy Scale	$\pm1\sigma(p_{\text{T}}, \eta, E, A)$	N & S	7.6%	all
Jet Energy Resolution	$\pm1\sigma(\lvert\eta\rvert)$	N & S	3.2%	all
Pileup	$\pm1\sigma(n_{\text{PV}})$	N & S	2.9%	all
Boosted μ+jets Trigger Eff.	$\pm1\sigma(p_{\text{T}}, \eta)$	N & S	0.4%	type-1/2 μ+jets
Resolved μ+jets Trigger Eff.	$\pm1\sigma(p_{\text{T}}, \eta)$	N & S	0.1%	type-3 μ+jets
Boosted e+jets Trigger Eff.	$\pm1\sigma(p_{\text{T}}, \lvert\eta\rvert)$	N & S	18.6%	type-1/2 e+jets
Resolved e+jets Trigger Eff.	$\pm1\sigma(p_{\text{T}}, \eta)$	N & S	2.5%	type-3 e+jets
Muon ID Eff.	$\pm1\sigma(p_{\text{T}}, \lvert\eta\rvert, n_{\text{PV}})$	N & S	0.4%	all μ+jets
Muon PF Isolation Eff.	$\pm1\sigma(p_{\text{T}}, \lvert\eta\rvert, n_{\text{PV}})$	N & S	0.2%	type-3 μ+jets
Electron ID Eff.	$\pm1\sigma(p_{\text{T}}, \lvert\eta\rvert)$	N & S	1.0%	all e+jets
b-tag Eff., b jets (Loose)	$\pm1\sigma(p_{\text{T}}, \eta)$	N & S	2.5%	type-1/2
b-tag Eff., c jets (Loose)	$\pm1\sigma(p_{\text{T}}, \eta)$	N & S	1.2%	type-1/2
b-tag Eff., light jets (Loose)	$\pm1\sigma(p_{\text{T}}, \eta)$	N & S	6.3%	type-1/2
b-tag Eff., b jets (Medium)	$\pm1\sigma(p_{\text{T}}, \eta)$	N & S	1.9%	type-3
b-tag Eff., c jets (Medium)	$\pm1\sigma(p_{\text{T}}, \eta)$	N & S	0.8%	type-3
b-tag Eff., light jets (Medium)	$\pm1\sigma(p_{\text{T}}, \eta)$	N & S	1.2%	type-3
t-tag Eff. (merged)	$\pm1\sigma(p_{\text{T}})$	N & S	1.6%	type-1
t-tag Eff. (semimerged)	$\pm1\sigma(p_{\text{T}})$	N & S	2.2%	type-1
t-tag Eff. (not merged)	$\pm1\sigma(p_{\text{T}})$	N & S	2.8%	type-1
ISR scale	$\pm1\sigma$	N & S	2.2%	$\text{t}\bar{\text{t}}$
FSR scale	$\pm1\sigma$	N & S	2.6%	$\text{t}\bar{\text{t}}$
ME-PS matching (h_{damp})	$\pm1\sigma$	N & S	2.5%	$\text{t}\bar{\text{t}}$
`CUETP8M2T4` tune	$\pm1\sigma$	N & S	2.4%	$\text{t}\bar{\text{t}}$
Color reconnection	$\pm1\sigma$	S	2.8%	$\text{t}\bar{\text{t}}$
b fragmentation	$\pm1\sigma(x_{\text{b}})$	N & S	3.7%	$\text{t}\bar{\text{t}}$
b branching ratio	$\pm1\sigma$	N & S	1.0%	$\text{t}\bar{\text{t}}$
top p_{T} reweighting	$\pm1\sigma(p_{\text{T}}^{\text{gen,t}}, p_{\text{T}}^{\text{gen,}\bar{\text{t}}})$	S	2.5%	$\text{t}\bar{\text{t}}$
PDF/α_S variation	NNPDF 3.0	S	1.5%	$\text{t}\bar{\text{t}}$
Renormalization scale μ_{R}	$\frac{1}{2}\mu_{\text{R}} \to 2\mu_{\text{R}}$	S	2.6%	$\text{t}\bar{\text{t}}$
Factorization scale μ_{F}	$\frac{1}{2}\mu_{\text{F}} \to 2\mu_{\text{F}}$	S	1.5%	$\text{t}\bar{\text{t}}$
Combined $\mu_{\text{R}}/\mu_{\text{F}}$ scale	$\frac{1}{2} \to 2(\mu_{\text{R}}/\mu_{\text{F}})$	S	3.8%	$\text{t}\bar{\text{t}}$ MC
Luminosity	$\pm2.5\%$	N	—	all
$R_{\text{q}\bar{\text{q}}}$	$\pm1\%$	N & S	—	all $f_{\text{qp}*}/f_{\text{qm}*}$
R_{Wjets}	$\pm10\%$	N	—	all W+jets MC
$R_{\text{QCD}}^{t/C/R}$ (20 params total)	$\pm1\sigma$ (stat)	N	—	QCD multijet

A template-based, binned likelihood combining the three-dimensional observable space in all channels and regions is constructed to compare observed data with expectation using a Poisson probability in each independent template bin as a function of the fit parameters of interest. Systematic uncertainties are accounted for as nuisance parameters in the likelihood, with variations for shape systematics accounted for by an interpolation between nominal and shifted

templates with a Gaussian prior and normalization systematics accounted for by log-normal priors. The total likelihood is maximized with respect to these parameters three times, allowing each parameter of interest to vary in independent investigations. Equation (7) is the template parameterization of the cross section for the $A_{\mathrm{FB}}^{(1)}$ fit, which assumes $d = \mu = 0$. Equation (9) is the template parameterization of the cross section used in the fits for d and μ, which assume $\mu = 0$ and $d = 0$, respectively, and $A_{\mathrm{FB}} = 0.036$ (the value from the $\mathrm{t\bar{t}}$ MC sample).

Final values of parameters of interest are determined from a Neyman construction [56] in which 1,000 toy datasets are generated from the models with given true values of a parameter of interest and then fit. The median and $\pm 1\sigma$ interval curves are plotted, and the parameter of interest's value is the true value in the toys whose postfit median was that of the value returned by the fit to data, interpolating linearly between points if necessary. The uncertainty intervals are constructed similarly from the $\pm 1\sigma$ curves.

7 Results

The application of the fitting procedure to the data samples yield the following values for the parameters of interest: $A_{\mathrm{FB}}^{(1)} = 0.048^{+0.088}_{-0.084}\,(\mathrm{stat}) \pm 0.028\,(\mathrm{syst})$, $d = 0.002 \pm 0.010\,(\mathrm{stat})^{+0.014}_{-0.019}\,(\mathrm{syst})$, and $\mu = -0.024^{+0.013}_{-0.007}\,(\mathrm{stat})^{+0.016}_{-0.006}\,(\mathrm{syst})$. Figure 6 shows the Neyman construction plots corresponding to these final values; the contour visible in the Neyman plot for the d parameter investigation is a result of an inherent sign ambiguity in the fitting function as detailed in Eq. (9). Figure 7 shows representative fit function comparison plots for the $A_{\mathrm{FB}}^{(1)}$analysis in each signal region channel, summed over lepton charge. Generally good agreement is observed, and results from the d and μ analyses are comparable.

The goodness of fit is evaluated using the Kolmogorov-Smirnov (KS) test statistic [57]. The value of the KS statistic, which quantifies the differences between the MC template and real data cumulative probability distributions, is smallest when the two distributions are most similar and the simulation describes the data well. The single values for the fits to real data are compared to the distributions of values observed for fits to groups of 1,000 toy MC datasets generated with floating values of the fit's parameters. Integrating each normalized KS test statistic distribution from its associated data fit value to infinity represents the "goodness" of the template fit to data in each channel in terms of a "p-value": the parameter-independent probability of the templates providing a poorer-than-observed description of the data. The p-values for each signal region channel and each parameter fit are presented in Table 2, where values nearer to unity indicate that the simulation describes the observed data as predictably as they describe arbitrary toy MC datasets.

The measured forward-backward asymmetry agrees with the most recent measurements from the Tevatron experiments [7–11], as well as with predictions from NLO QCD [3–5] and NNLO QCD [6]. The statistical uncertainty is somewhat diminished by the coarser than ideal binning of the template function that was required to accommodate the relatively lower numbers of generated events in some of the simulated samples needed to evaluate systematic uncertainties. The measured anomalous chromoelectric and chromomagnetic moments are consistent with zero.

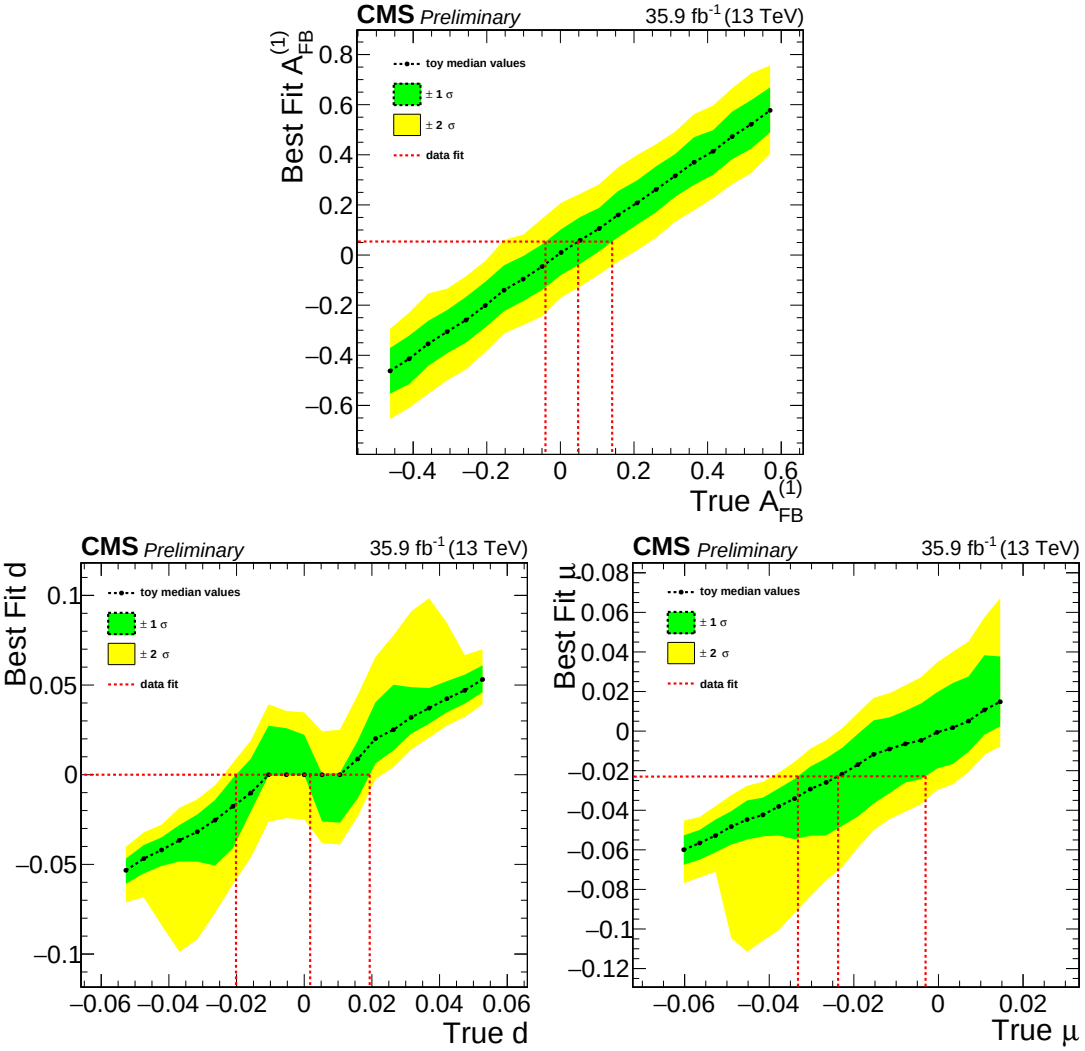

Figure 6: Neyman constructions for the $A_{\mathrm{FB}}^{(1)}$(top), d (bottom left) and μ (bottom right) parameters of interest considering groups of 1,000 toys generated with systematic uncertainty nuisance parameters floating. The horizontal red lines indicate the values of the parameters determined by the fits and the vertical red lines indicate where these values intersect with the central value and uncertainty curves from the toy groups.

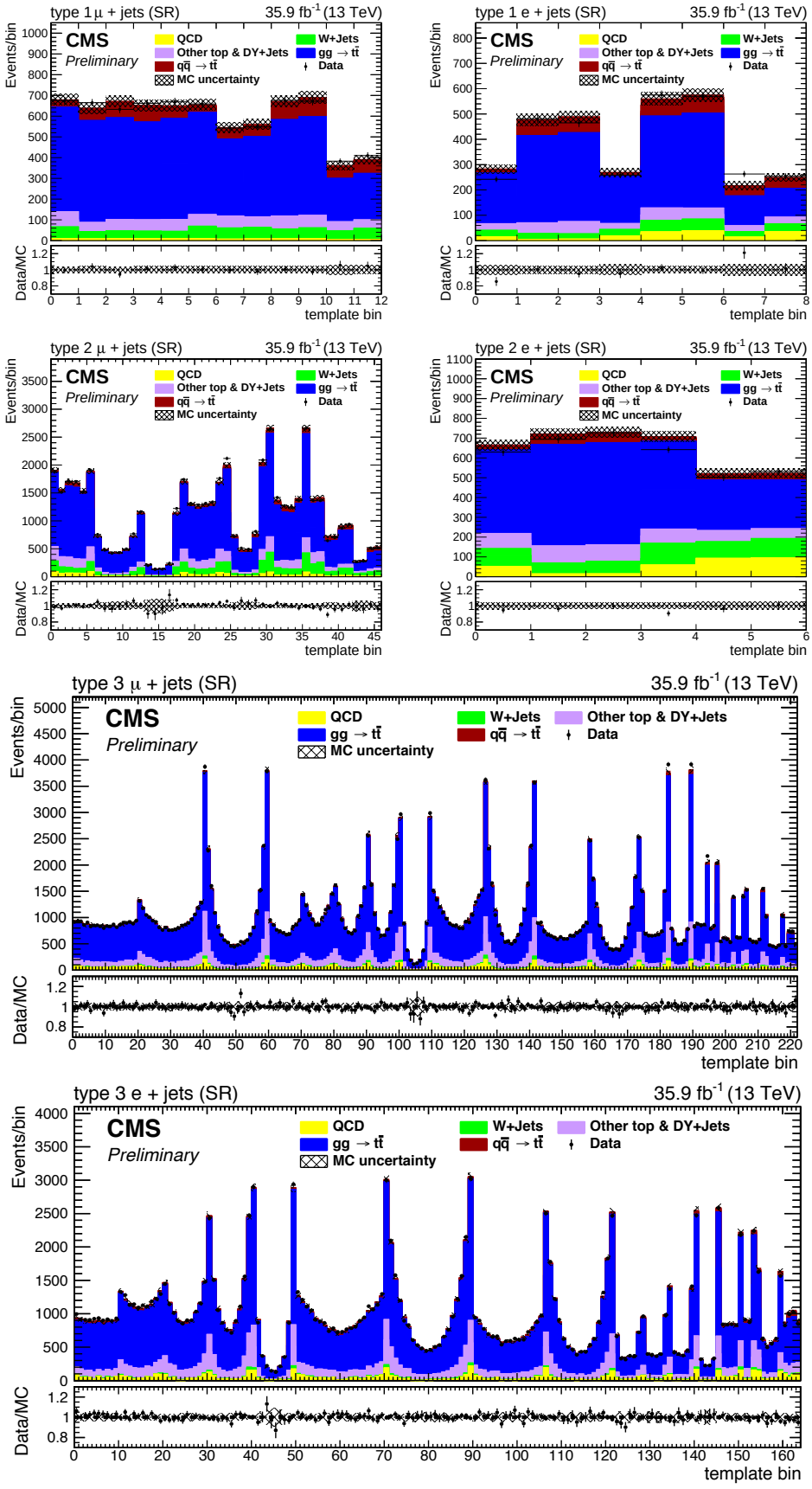

Figure 7: Postfit data/MC comparisons as functions of template bin number for the $A_{\mathrm{FB}}^{(1)}$ parameter investigation. The top four plots show events in the type-1 (top row) and type-2 (second row) μ +jets (left column) and e +jets (right column) channels, and the bottom two plots show events in the type-3 μ +jets (third row) and e +jets (bottom row) channels, summed over lepton charge in all cases.

Table 2: Observed p-values representing channel-dependent goodness of fit

Channel	$A_{\mathrm{FB}}^{(1)}$ **fit** p**-value**	d **fit** p**-value**	μ **fit** p**-value**
type-1 μ +jets ($Q>0$)	0.688	1.000	1.000
type-1 μ +jets ($Q<0$)	0.971	0.932	0.976
type-1 e +jets ($Q>0$)	0.643	1.000	1.000
type-1 e +jets ($Q<0$)	0.125	0.892	0.881
type-2 μ +jets ($Q>0$)	0.163	1.000	1.000
type-2 μ +jets ($Q<0$)	0.090	1.000	1.000
type-2 e +jets ($Q>0$)	0.669	0.585	0.646
type-2 e +jets ($Q<0$)	0.775	0.943	0.970
type-3 μ +jets ($Q>0$)	0.686	1.000	1.000
type-3 μ +jets ($Q<0$)	0.771	1.000	1.000
type-3 e +jets ($Q>0$)	0.088	0.911	0.972
type-3 e +jets ($Q<0$)	0.102	0.954	0.992

8 Summary

The linearized parton-level top quark forward-backward asymmetry $A_{\mathrm{FB}}^{(1)}$ and anomalous chromoelectric (d) and chromomagnetic (μ) moments have been measured in $35.9\,\mathrm{fb}^{-1}$ of LHC proton-proton collision data collected with the CMS detector in 2016 at a center-of-mass energy of 13 TeV. Candidate $\mathrm{t\bar{t}}$ events decaying to lepton plus jets final states with "resolved" (low-momentum) and "boosted" (high-momentum) topologies were selected and their top quark candidate pairs were reconstructed using a kinematic fit of the decay products to $\mathrm{t\bar{t}}$ hypotheses. Parameters of interest have been measured using template-based likelihood fits to observed data of differential models based on extensions to tree-level cross sections for quark-antiquark and gluon-gluon initial states, and are determined to be $A_{\mathrm{FB}}^{(1)} = 0.048^{+0.088}_{-0.084}\,(\mathrm{stat}) \pm 0.028\,(\mathrm{syst})$, $d = 0.002 \pm 0.010\,(\mathrm{stat})^{+0.014}_{-0.019}\,(\mathrm{syst})$, and $\mu = -0.024^{+0.013}_{-0.007}\,(\mathrm{stat})^{+0.016}_{-0.006}\,(\mathrm{syst})$.

References

[1] Q.-H. Cao et al., "Forward-backward asymmetry of top quark pair production", *Phys. Rev. D* **81** (2010) 114004, doi:10.1103/PhysRevD.81.114004, arXiv:1003.3461.

[2] M. I. Gresham, I.-W. Kim, and K. M. Zurek, "On models of new physics for the Tevatron top A_{FB}", *Phys. Rev. D* **83** (2011) 114027, doi:10.1103/PhysRevD.83.114027, arXiv:1103.3501.

[3] J. H. Kühn and G. Rodrigo, "Charge asymmetry of heavy quarks at hadron colliders", *Phys. Rev. D* **59** (1999) 054017, doi:10.1103/PhysRevD.59.054017, arXiv:hep-ph/9807420.

[4] J. H. Kühn and G. Rodrigo, "Charge asymmetries of top quarks at hadron colliders revisited", *JHEP* **01** (2012) 063, doi:10.1007/JHEP01(2012)063, arXiv:1109.6830.

[5] J. A. Aguilar-Saavedra, W. Bernreuther, and Z. G. Si, "Collider-independent top quark forward-backward asymmetries: standard model predictions", *Phys. Rev. D* **86** (2012) 115020, doi:10.1103/PhysRevD.86.115020, arXiv:1209.6352.

[6] M. Czakon, P. Fiedler, and A. Mitov, "Resolving the Tevatron Top Quark Forward-Backward Asymmetry Puzzle: Fully Differential Next-to-Next-to-Leading-Order Calculation", *Phys. Rev. Lett.* **115** (2015) 052001, doi:10.1103/PhysRevLett.115.052001, arXiv:1411.3007.

[7] CDF Collaboration, "Evidence for a mass dependent forward-backward asymmetry in top quark pair production", *Phys. Rev. D* **83** (2011) 112003, doi:10.1103/PhysRevD.83.112003, arXiv:1101.0034.

[8] D0 Collaboration, "First measurement of the forward-backward charge asymmetry in top quark pair production", *Phys. Rev. Lett.* **100** (2008) 142002, doi:10.1103/PhysRevLett.100.142002, arXiv:0712.0851.

[9] D0 Collaboration, "Measurement of the forward-backward asymmetry in top quark-antiquark production in $\mathrm{p\bar{p}}$ collisions using the lepton+jets channel", *Phys. Rev. D* **90** (2014) 072011, doi:10.1103/PhysRevD.90.072011, arXiv:1405.0421.

[10] CDF Collaboration, "Measurement of the forward-backward asymmetry of top-quark and antiquark pairs using the full CDF Run II data set", *Phys. Rev. D* **93** (2016) 112005, doi:10.1103/PhysRevD.93.112005, arXiv:1602.09015.

[11] CDF and D0 Collaborations, "Combined forward-backward asymmetry measurements in top-antitop quark production at the Tevatron", *Phys. Rev. Lett.* **120** (2018) 042001, doi:10.1103/PhysRevLett.120.042001, arXiv:1709.04894.

[12] CMS Collaboration, "Measurement of the charge asymmetry in top-quark pair production in proton-proton collisions at $\sqrt{s} = 7$ TeV", *Phys. Lett. B* **709** (2012) 28, doi:10.1016/j.physletb.2012.01.078, arXiv:1112.5100.

[13] CMS Collaboration, "Measurements of the $\mathrm{t\bar{t}}$ charge asymmetry using the dilepton decay channel in pp collisions at $\sqrt{s} = 7$ TeV", *JHEP* **04** (2014) 191, doi:10.1007/JHEP04(2014)191, arXiv:1402.3803.

[14] CMS Collaboration, "Measurement of the charge asymmetry in top quark pair production in pp collisions at $\sqrt{s} = 8$ TeV using a template method", *Phys. Rev. D* **93** (2016) 034014, doi:10.1103/PhysRevD.93.034014, arXiv:1508.03862.

[15] CMS Collaboration, "Measurements of $\mathrm{t\bar{t}}$ charge asymmetry using dilepton final states in pp collisions at $\sqrt{s} = 8$ TeV", *Phys. Lett. B* **760** (2016) 365, doi:10.1016/j.physletb.2016.07.006, arXiv:1603.06221.

[16] ATLAS Collaboration, "Measurement of the charge asymmetry in top quark pair production in pp collisions at $\sqrt{s} = 7$ TeV using the ATLAS detector", *Eur. Phys. J. C* **72** (2012) 2039, doi:10.1140/epjc/s10052-012-2039-5, arXiv:1203.4211.

[17] ATLAS Collaboration, "Measurement of the charge asymmetry in highly boosted top-quark pair production in $\sqrt{s} = 8$ TeV pp collision data collected by the ATLAS experiment", *Phys. Lett. B* **756** (2016) 52, doi:10.1016/j.physletb.2016.02.055, arXiv:1512.06092.

[18] D. Atwood, A. Aeppli, and A. Soni, "Extracting anomalous gluon-top effective couplings at the supercolliders", *Phys. Rev. Lett.* **69** (1992) 2754, doi:10.1103/PhysRevLett.69.2754.

[19] D. Atwood, A. Kagan, and T. G. Rizzo, "Constraining anomalous top quark couplings at the Tevatron", *Phys. Rev. D* **52** (1995) 6264, doi:10.1103/PhysRevD.52.6264, arXiv:hep-ph/9407408.

[20] P. Haberl, O. Nachtmann, and A. Wilch, "Top production in hadron hadron collisions and anomalous top-gluon couplings", *Phys. Rev. D* **53** (1996) 4875, doi:10.1103/PhysRevD.53.4875, arXiv:hep-ph/9505409.

[21] K.-M. Cheung, "Probing the chromoelectric and chromomagnetic dipole moments of the top quark at hadronic colliders", *Phys. Rev. D* **53** (1996) 3604, doi:10.1103/PhysRevD.53.3604, arXiv:hep-ph/9511260.

[22] CMS Collaboration, "Measurements of $\mathrm{t\bar{t}}$ spin correlations and top quark polarization using dilepton final states in pp collisions at $\sqrt{s} = 8$ TeV", *Phys. Rev. D* **93** (2016) 052007, doi:10.1103/PhysRevD.93.052007, arXiv:1601.01107.

[23] P. Nason, "A New method for combining NLO QCD with shower Monte Carlo algorithms", *JHEP* **11** (2004) 040, doi:10.1088/1126-6708/2004/11/040, arXiv:hep-ph/0409146.

[24] S. Frixione, P. Nason, and C. Oleari, "Matching NLO QCD computations with Parton Shower simulations: the POWHEG method", *JHEP* **11** (2007) 070, doi:10.1088/1126-6708/2007/11/070, arXiv:0709.2092.

[25] S. Alioli, P. Nason, C. Oleari, and E. Re, "A general framework for implementing NLO calculations in shower Monte Carlo programs: the POWHEG BOX", *JHEP* **06** (2010) 043, doi:10.1007/JHEP06(2010)043, arXiv:1002.2581.

[26] J. C. Collins and D. E. Soper, "Angular distribution of dileptons in high-energy hadron collisions", *Phys. Rev. D* **16** (1977) 2219, doi:10.1103/PhysRevD.16.2219.

[27] CMS Collaboration, "CMS luminosity measurements for the 2016 data taking period", CMS Physics Analysis Summary CMS-PAS-LUM-17-001, 2017.

[28] S. Frixione, P. Nason, and G. Ridolfi, "A positive-weight next-to-leading-order Monte Carlo for heavy flavour hadroproduction", *JHEP* **09** (2007) 126, doi:10.1088/1126-6708/2007/09/126, arXiv:0707.3088.

[29] T. Sjöstrand et al., "An Introduction to PYTHIA 8.2", *Comput. Phys. Commun.* **191** (2015) 159, doi:10.1016/j.cpc.2015.01.024, arXiv:1410.3012.

[30] CMS Collaboration, "Investigations of the impact of the parton shower tuning in Pythia 8 in the modelling of $\mathrm{t\bar{t}}$ at $\sqrt{s} = 8$ and 13 TeV", CMS Physics Analysis Summary CMS-PAS-TOP-16-021, 2016.

[31] A. Kalogeropoulos and J. Alwall, "The SysCalc code: A tool to derive theoretical systematic uncertainties", arXiv:1801.08401.

[32] M. Cacciari et al., "The $\mathrm{t\bar{t}}$ cross-section at 1.8 TeV and 1.96 TeV: A study of the systematics due to parton densities and scale dependence", *JHEP* **04** (2004) 068, doi:10.1088/1126-6708/2004/04/068, arXiv:hep-ph/0303085.

[33] S. Catani, D. de Florian, M. Grazzini, and P. Nason, "Soft gluon resummation for Higgs boson production at hadron colliders", *JHEP* **07** (2003) 028, doi:10.1088/1126-6708/2003/07/028, arXiv:hep-ph/0306211.

[34] NNPDF Collaboration, "Parton distributions for the LHC Run II", *JHEP* **04** (2015) 040, doi:10.1007/JHEP04(2015)040, arXiv:1410.8849.

[35] S. Alioli, P. Nason, C. Oleari, and E. Re, "NLO single-top production matched with shower in POWHEG: s- and t-channel contributions", *JHEP* **09** (2009) 111, doi:10.1007/JHEP02(2010)011,10.1088/1126-6708/2009/09/111, arXiv:0907.4076. [Erratum: JHEP02,011(2010)].

[36] P. Artoisenet, R. Frederix, O. Mattelaer, and R. Rietkerk, "Automatic spin-entangled decays of heavy resonances in Monte Carlo simulations", *JHEP* **03** (2013) 015, doi:10.1007/JHEP03(2013)015, arXiv:1212.3460.

[37] E. Re, "Single-top Wt-channel production matched with parton showers using the POWHEG method", *Eur. Phys. J. C* **71** (2011) 1547, doi:10.1140/epjc/s10052-011-1547-z, arXiv:1009.2450.

[38] S. Frixione and B. R. Webber, "Matching NLO QCD computations and parton shower simulations", *JHEP* **06** (2002) 029, doi:10.1088/1126-6708/2002/06/029, arXiv:hep-ph/0204244.

[39] J. Alwall et al., "The automated computation of tree-level and next-to-leading order differential cross sections, and their matching to parton shower simulations", *JHEP* **07** (2014) 079, doi:10.1007/JHEP07(2014)079, arXiv:1405.0301.

[40] J. Alwall et al., "Comparative study of various algorithms for the merging of parton showers and matrix elements in hadronic collisions", *Eur. Phys. J. C* **53** (2008) 473, doi:10.1140/epjc/s10052-007-0490-5, arXiv:0706.2569.

[41] GEANT4 Collaboration, "GEANT4: a simulation toolkit", *Nucl. Instrum. Meth. A* **506** (2003) 250, doi:10.1016/S0168-9002(03)01368-8.

[42] P. Kant et al., "HatHor for single top-quark production: Updated predictions and uncertainty estimates for single top-quark production in hadronic collisions", *Comput. Phys. Commun.* **191** (2015) 74, doi:10.1016/j.cpc.2015.02.001, arXiv:1406.4403.

[43] N. Kidonakis, "Two-loop soft anomalous dimensions for single top quark associated production with a W or H", *Phys. Rev. D* **82** (2010) 054018, doi:10.1103/PhysRevD.82.054018, arXiv:1005.4451.

[44] R. Gavin, Y. Li, F. Petriello, and S. Quackenbush, "FEWZ 2.0: A code for hadronic Z production at next-to-next-to-leading order", *Comput. Phys. Commun.* **182** (2011) 2388, doi:10.1016/j.cpc.2011.06.008, arXiv:1011.3540.

[45] M. Czakon and A. Mitov, "Top++: a program for the calculation of the top pair cross section at hadron colliders", *Comput. Phys. Commun.* **185** (2014) 2930, doi:10.1016/j.cpc.2014.06.021, arXiv:1112.5675.

[46] J. Thaler and K. Van Tilburg, "Identifying boosted objects with N-subjettiness", *JHEP* **03** (2011) 015, doi:10.1007/JHEP03(2011)015, arXiv:1011.2268.

[47] CMS Collaboration, "Identification of heavy-flavour jets with the CMS detector in pp collisions at 13 TeV", *JINST* **13** (2018) P05011, doi:10.1088/1748-0221/13/05/P05011, arXiv:1712.07158.

[48] J. Erdmann et al., "A likelihood-based reconstruction algorithm for top-quark pairs and the KLFitter framework", *Nucl. Instrum. Meth. A* **748** (2014) 18, doi:10.1016/j.nima.2014.02.029, arXiv:1312.5595.

[49] F. James and M. Roos, "Minuit: a system for function minimization and analysis of the parameter errors and correlations", *Comput. Phys. Commun.* **10** (1975) 343, doi:10.1016/0010-4655(75)90039-9.

[50] M. Czakon et al., "Top-pair production at the LHC through NNLO QCD and NLO EW", *JHEP* **10** (2017) 186, doi:10.1007/JHEP10(2017)186, arXiv:1705.04105.

[51] CMS Collaboration, "Search for new physics in top quark production in dilepton final states in proton-proton collisions at $\sqrt{s}$ = 13 TeV", arXiv:1903.11144.

[52] J. Butterworth et al., "PDF4LHC recommendations for LHC Run II", *J. Phys. G* **43** (2016) 023001, doi:10.1088/0954-3899/43/2/023001, arXiv:1510.03865.

[53] J. Rojo et al., "The PDF4LHC report on PDFs and LHC data: Results from Run I and preparation for Run II", *J. Phys. G* **42** (2015) 103103, doi:10.1088/0954-3899/42/10/103103, arXiv:1507.00556.

[54] A. Accardi et al., "A critical appraisal and evaluation of modern PDFs", *Eur. Phys. J. C* **76** (2016) 471, doi:10.1140/epjc/s10052-016-4285-4, arXiv:1603.08906.

[55] R. J. Barlow and C. Beeston, "Fitting using finite Monte Carlo samples", *Comput. Phys. Commun.* **77** (1993) 219, doi:10.1016/0010-4655(93)90005-W.

[56] J. Neyman, "Outline of a theory of statistical estimation based on the classical theory of probability", *Philos. Trans. Royal Soc. A* **236** (1937) 333.

[57] F. J. Massey Jr., "The Kolmogorov-Smirnov test for goodness of fit", *J. Am. Stat. Assoc.* **46** (1951) 68, doi:10.1080/01621459.1951.10500769.

A Appendix 1: Reweighting Factors

The five parameter independent template functions $f_{gn}(\vec{y})$ that are defined in Eq. (9) are constructed from fully simulated gg initiated [includes qg, qq, $\bar{q}\bar{q}$, $q_i\bar{q}_j$ ($i \neq j$)] events at NLO using the following weights,

$$w_{g0}(m^2_{t\bar{t}}, c^*) = 1 \tag{10}$$

$$w_{g1}(m^2_{t\bar{t}}, c^*) = \frac{1}{B(c^*, \beta)\,(1 + \varepsilon\beta^2 c^{*2})} \tag{11}$$

$$w_{g2}(m^2_{t\bar{t}}, c^*) = \frac{56}{(1-\beta^2)\,A(c^*, \beta)B(c^*, \beta)\,(1 + \varepsilon\beta^2 c^{*2})} \tag{12}$$

$$w_{g3}(m^2_{t\bar{t}}, c^*) = \frac{4}{(1-\beta^2 c_*^2)\,A(c^*, \beta)B(c^*, \beta)\,(1 + \varepsilon\beta^2 c^{*2})} \tag{13}$$

$$w_{g4}(m^2_{t\bar{t}}, c^*) = \frac{8}{A(c^*, \beta)B(c^*, \beta)\,(1 + \varepsilon\beta^2 c^{*2})} \cdot \left(\frac{1}{1-\beta^2 c_*^2} + \frac{1}{1-\beta^2} + \frac{4(1-\beta^2 c_*^2)}{(1-\beta^2)^2}\right) \tag{14}$$

where the functions A and B are defined as

$$A(c^*, \beta) = \frac{7 + 9\beta^2 c^{*2}}{1 - \beta^2 c^{*2}} \tag{15}$$

$$B(c^*, \beta) = \frac{1 - \beta^4 c^{*4} + 2\beta^2(1-\beta^2)(1-c^{*2})}{2(1-\beta^2 c^{*2})} \tag{16}$$

The three parameter independent template functions $f_{qn}(\vec{y})$ that are defined in Eq. (9) are constructed from fully simulated $q\bar{q}$ initiated events at NLO using the following weights,

$$w_{q0}(m^2_{t\bar{t}}, c^*) = 1 \tag{17}$$

$$w_{q1}(m^2_{t\bar{t}}, c^*) = \frac{4}{1 + \beta^2 c^{*2} + (1-\beta^2) + \alpha\,(1 - \beta^2 c^{*2})} \tag{18}$$

$$w_{q2}(m^2_{t\bar{t}}, c^*) = \frac{4}{1 + \beta^2 c^{*2} + (1-\beta^2) + \alpha\,(1 - \beta^2 c^{*2})} \cdot \frac{1 - \beta^2 c^{*2}}{1 - \beta^2} \tag{19}$$

$$\tag{20}$$

The distribution functions are normalized as follows,

$$\int d^4y f_{bk}(\vec{y}) = \sum_Q \int dx_r dm_r dc_r f_{bk}(x_r, m_r, c_r, Q) = 1 \tag{21}$$

$$\int d^4y f_{g0}(\vec{y}) = \sum_Q \int dx_r dm_r dc_r f_{g0}(x_r, m_r, c_r, Q) = 1 \tag{22}$$

$$\int d^4y f_{q0}(\vec{y}) = \sum_Q \int dx_r dm_r dc_r f_{q0}(x_r, m_r, c_r, Q) = 1 \tag{23}$$

and the functions F_{gn} and F_{qn} are the integrals of the reweighted functions f_{gn} and f_{qn} for $\mathrm{n} > 0$,

$$F_{\mathrm{gn}} = \int d^4y f_{\mathrm{gn}}(\vec{y}) = \sum_Q \int dx_{\mathrm{r}} dm_{\mathrm{r}} dc_{\mathrm{r}} f_{\mathrm{gn}}(x_{\mathrm{r}}, m_{\mathrm{r}}, c_{\mathrm{r}}, Q) \tag{24}$$

$$F_{\mathrm{qn}} = \int d^4y f_{\mathrm{qn}}(\vec{y}) = \sum_Q \int dx_{\mathrm{r}} dm_{\mathrm{r}} dc_{\mathrm{r}} f_{\mathrm{qn}}(x_{\mathrm{r}}, m_{\mathrm{r}}, c_{\mathrm{r}}, Q). \tag{25}$$

These are then used to define the normalization factors in Eq. (9),

$$F_{\mathrm{gg}}(\mu, d) = 1 + \mu(1+\mu)F_{\mathrm{g1}} + (\mu^2 + d^2)(1+\mu)F_{\mathrm{g2}} + (\mu^2 + d^2)(1-5\mu)F_{\mathrm{g3}} + (\mu^2 + d^2)^2 F_{\mathrm{g4}} \tag{26}$$

$$F_{\mathrm{q\bar{q}}}(\mu, d) = 1 + \left(2\mu + \mu^2 - d^2\right) F_{\mathrm{q1}} + \left(\mu^2 + d^2\right) F_{\mathrm{q2}} \tag{27}$$